

Large-scale ice-shelf calving events follow prolonged amplifications in flexure

Received: 28 June 2024

Accepted: 30 April 2025

Published online: 1 July 2025

 Check for updates

Nathan J. Teder¹, Luke G. Bennetts^{1,2}✉, Phillip A. Reid^{3,4},
Robert A. Massom^{4,5,6}, Jordan P. A. Pitt⁷, Theodore A. Scambos⁸ &
Alexander D. Fraser⁴

The retreat of Antarctic ice shelves due to calving and the subsequent reduction in buttressing of the Antarctic Ice Sheet are of major concern for future sea-level rise. Sudden, widespread calving of weakened ice shelves has been linked to fracture amplification forced by ocean swell following regional sea-ice losses, but increases in the magnitudes and durations of swell-induced ice-shelf flexure in the lead-ups to calving events have not been tracked. Here we present 7-year datasets of sea-ice-barrier lengths and shelf-front flexural stress that encompass large-scale calving events for the Wilkins and Voyeykov ice shelves. We find that the ice shelves exhibit similar preconditioning patterns, characterized by prolonged amplifications in flexure and the collapse of adjoining fast-ice barriers. We propose a conceptual model for the swell–sea-ice–shelf-front conditions that lead to calving events, show that it fits other major calving events and discuss the likely importance of sea-ice loss for the future of ice shelves.

In an equilibrium climate state, iceberg calving from ice shelves is a natural process that balances mass gain from glacial inflow. In the era of climate change, Antarctic ice shelves are suffering major mass losses due to melting and calving^{1–3}, thus reducing their vital ability to buttress Antarctic Ice Sheet outflow^{4,5}. Over the past three decades, multiple small-to-medium ice shelves have experienced large-scale calving events that removed $\geq 10\%$ of their areas over periods of just days to weeks^{6–10}. Prominent calving events around the Antarctic Peninsula led to ice-shelf disintegrations^{6,7,11} that are probably connected with severe previous warming of the region^{12,13} and associated sea-ice loss¹¹. As warmer temperatures spread around the Antarctic coastline, there is an urgent need to understand the wider vulnerability of ice shelves to sea-ice loss^{11,14} to reduce the substantial uncertainties in sea-level projections¹⁵.

Massom et al.¹¹ connected the Antarctic Peninsula disintegration events with regional sea-ice losses, as sea ice attenuates swell^{16,17} and (land)fast ice provides backstress that bolsters ice shelves^{9–11,18}.

They proposed that, without an effective sea-ice barrier, energetic swell repeatedly flexed the damaged outer shelf margins, amplifying fractures until they calved. Sea-ice losses and swell flexure have since been implicated in calving events across Antarctica^{9,19–21}, but there are few direct measurements of ice-shelf flexure^{22–24} and no model assessments of pre-calving flexure have been performed to empower predictions of future events.

In this Article, we present time series of flexural stress experienced by the Voyeykov and Wilkins ice shelves that advance our understanding of their large-scale calving events in 2007 and 2008, respectively (Fig. 1). To achieve this, we analyse satellite data from September 2002–August 2009 to quantify the pack- and fast-ice barriers^{25,26} and model attenuation of the incoming swell^{27,28} and the flexural stress imposed on the shelf fronts^{29,30}. On the basis of our findings, we propose a conceptual model of the prolonged amplifications in flexure that precondition large-scale calving of weakened shelf fronts, and relate the model to other ice shelves (see Fig. 5).

¹University of Adelaide, Adelaide, South Australia, Australia. ²The University of Melbourne, Melbourne, Victoria, Australia. ³Australian Bureau of Meteorology, Hobart, Tasmania, Australia. ⁴Australian Antarctic Program Partnership, Institute for Marine and Antarctic Studies, University of Tasmania, Hobart, Tasmania, Australia. ⁵Australian Antarctic Division, Kingston, Tasmania, Australia. ⁶Australian Centre for Excellence in Antarctic Science, Institute for Marine and Antarctic Studies, University of Tasmania, Hobart, Tasmania, Australia. ⁷University of Sydney, Sydney, New South Wales, Australia. ⁸University of Colorado, Boulder, CO, USA. ✉e-mail: luke.bennetts@unimelb.edu.au

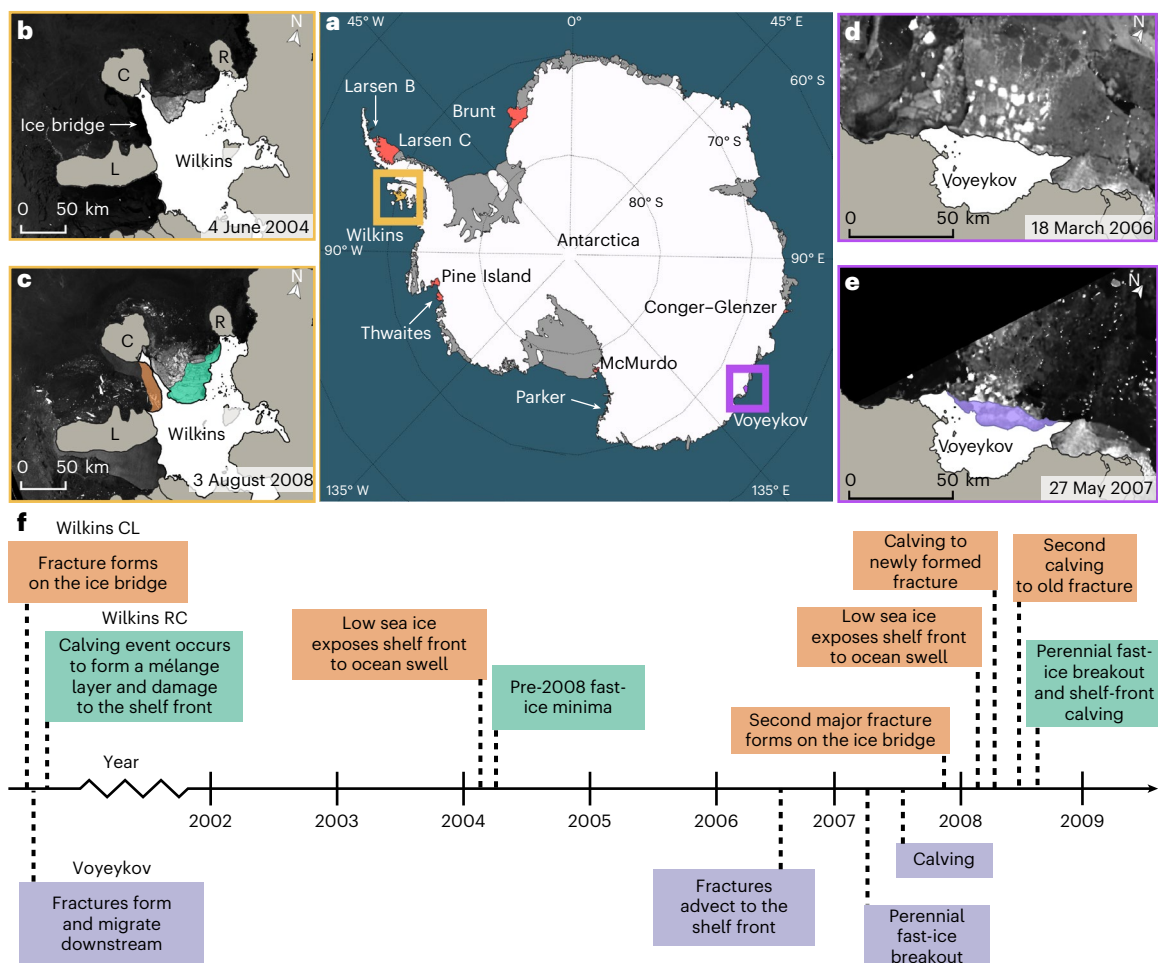


Fig. 1 | Large-scale calving of the Wilkins and Voyeykov ice shelves. **a**, Map of Antarctica showing the locations of the studied ice shelves, including ice shelves used only for the results in Fig. 5b (shaded red). **b–e**, Environmental Satellite (ENVISAT) Advanced Synthetic Aperture Radar (ASAR) Wide Swath Medium Resolution (WSM) imagery of the Wilkins Ice Shelf (**b,c**, indicated by the yellow box in **a**) and Voyeykov Ice Shelf (**d,e**, indicated by the purple box

in **a**) before (**b,d**) and after (**c,e**) the large-scale calving events. The islands dividing the Wilkins shelf front are labelled: Rothschild Island (R), Charcot Island (C) and Lataday Island (L). Areas lost to calving are indicated (green shading for Wilkins RC, orange for Wilkins CL and purple for Voyeykov). **f**, Timeline of the lead-ups to the large-scale calving events, colour coded according to the shelf front.

Exposure of damaged outer shelf margins to swell

The eastern section of the Voyeykov Ice Shelf was heavily fractured over the duration of analysed satellite images (from September 2002). The fractures propagated towards the shelf front before it calved in late April 2007 (Fig. 2a–c) in an event that removed 14% of its area over 4–5 days (ref. 9). The Wilkins shelf front is divided into distinct sections by islands (Rothschild Island, Charcot Island and Latady Island; Fig. 1b,c). The two fronts investigated are referred to as the Wilkins RC (Fig. 2d–f) and Wilkins CL (Fig. 2g–i), according to the bounding islands. The Wilkins RC suffered a large calving event in 1998^{7,31}, but many icebergs subsequently refroze to the shelf front in a mélange layer³², which supported the heavily damaged shelf-front region. In contrast, the Wilkins CL existed along an ice bridge with only one major fracture for the majority of the analysed period (Fig. 2g–i, gold curve). A 52-km-long fracture formed closer to the Wilkins CL front in July 2007 (Fig. 2i, purple curve)^{7,33}, along which it calved in late February 2008 and then along the previous fracture in late May 2008, removing a combined area of 650 km². The Wilkins RC then calved in late June 2008, with an area of 1,480 km² lost over two weeks. In total, the calving events removed 17% of the Wilkins³¹. The Bedmap2 dataset³⁴ implies that both ice shelves were <100 m thick in the areas that calved, indicating that swell has the potential to dominate ice-shelf stress^{35,36}.

Over the 7-year record, each shelf front was typically protected by an inner fast-ice barrier extending tens of kilometres from the shelf front, followed by an outer pack-ice barrier extending tens to hundreds of kilometres. Before the calving events, perennial fast ice made up nearly all of the Voyeykov fast-ice barrier (Fig. 2a,b) and a major proportion of the Wilkins RC fast-ice barrier (Fig. 2d,e). The perennial fast-ice barriers for the Voyeykov and Wilkins RC persisted even in periods with relatively low sea-ice extents, such as around the Wilkins in summer 2004 (Figs. 2g and 3f). Annual fast ice constitutes almost all of the Wilkins CL fast-ice barrier (Fig. 2h). During late summer 2004, the Wilkins CL lost its fast-ice barrier for 5 months, in addition to losing the majority of its pack-ice barrier, creating a wide corridor for ocean swell to reach the shelf front (Fig. 2g). This was the longest duration of exposure of the Wilkins CL to the open ocean over the analysed record before the calving event (compare the numbers of low sea-ice days in Fig. 3c).

In the months leading up to the calving events, each of the three shelf fronts experienced increasing exposure to the open ocean through reduced or diminished sea-ice barriers. Four months before the Voyeykov calving, its pack-ice and annual fast-ice barriers retreated rapidly due to cyclonic conditions and strong katabatic winds⁹, and in late March 2007 the perennial fast ice attached the eastern side of the shelf front broke-up (Figs. 2c and 3d,e). In the lead-up

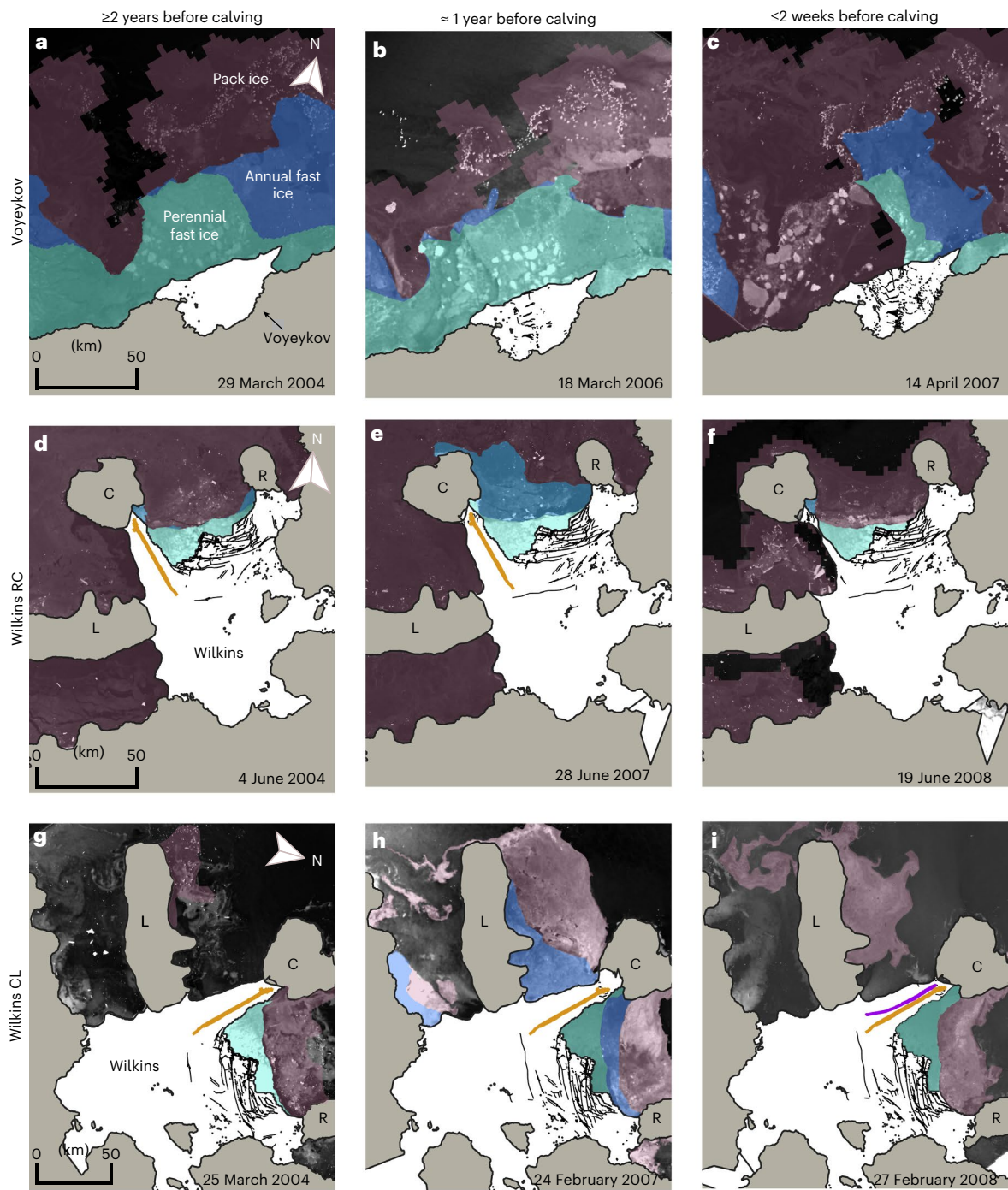


Fig. 2 | Sea-ice and shelf-front conditions in the years before large-scale calving events. **a–i**, Sea-ice types and ice-shelf damage superimposed on ENVISAT ASAR WSM imagery from daily Advanced Microwave Scanning Radiometer for EOS (AMSR-E) ARTIST sea-ice (ASI) dataset and fast-ice extent from ref. 25 (Methods) for the Voyeykov (**a–c**), Wilkins RC (**d–f**) and Wilkins CL (**g–i**). The images are oriented so that the relevant shelf front points upwards. For each shelf front, the

images shown were taken at similar periods before the respective calving events: in the low sea-ice year 2004 (**a,d,g**), the year before (**b,e,h**) and dates less than 2 weeks before (**c,f,i**). Fractures are superimposed on the ice shelves (thin black curves), with two Wilkins CL fractures along which calving occurred highlighted (thick gold and purple curves).

to the Wilkins calving events, the formation of La Niña and a persistent deep Admundsen Sea low drove surrounding sea-ice loss^{37–40}. Thus, the Wilkins CL had no fast-ice barrier and the least pack ice since 2004 in the 2 weeks before its first calving event (Fig. 2i; compare with Fig. 3h)¹¹. The Wilkins RC perennial fast ice survived the initial pack-ice loss, but the record high temperatures during early winter 2008³⁹ compounded the initial loss of the pack-ice and annual fast-ice barriers, such that the perennial fast-ice layer eventually broke away from the shelf front (Fig. 2f).

Prolonged reductions in sea-ice barriers

Over the record, each shelf front experiences the greatest number of days with a total effective sea-ice length $L_{\text{tot}} \equiv L_{\text{pck}} + L_{\text{ann}} + L_{\text{per}} \leq 100$ km (where L_{pck} is the effective pack-ice length, L_{ann} is the annual fast-ice length and L_{per} is the perennial pack-ice length; a value of $L_{\text{tot}} > 100$ km reduces the height of a 12 s swell by >90%) combined with a high number of days with $L_{\text{pck}} \leq 50$ km (the e-folding length for a 12 s swell) in the years of the calving events (years are September–August; Fig. 3a–c). For the Voyeykov, the large number of low sea-ice days in

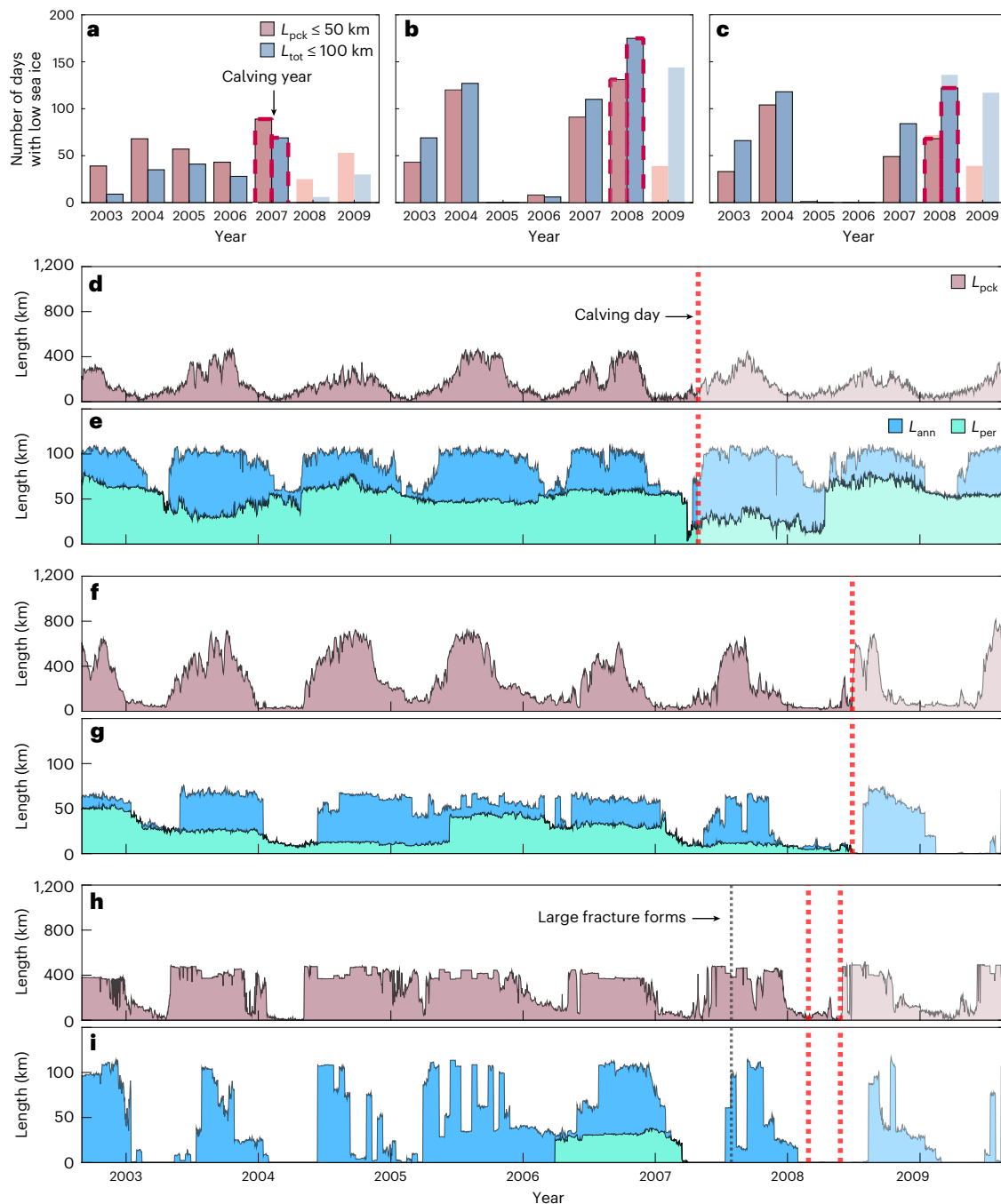


Fig. 3 | Sea-ice lengths over 2003–2009. **a–c**, Yearly count of low sea-ice days ($L_{pck} \leq 50$ km, $L_{tot} \leq 100$ km) for the Voyeykov (**a**), Wilkins RC (**b**) and Wilkins CL (**c**) (years are September–August). **d–i**, Daily time-series of effective sea-ice lengths for L_{pck} (**d,f,h**) and L_{ann} and L_{per} (**e,g,i**) for the Voyeykov (**d,e**), Wilkins RC (**f,g**)

and Wilkins CL (**h,i**). The sea-ice lengths shown are means for the lowest 33% of transects for a particular shelf front on a given day (Methods). The lighter shaded regions are after the calving events (the second calving event for the Wilkins CL).

2007 is caused by a sharp drop in (effective) pack-ice length (Fig. 3d) starting in November 2006 (<6 months before calving) and a drop in annual fast-ice length (Fig. 3e) starting shortly afterwards. The perennial fast ice attached to the eastern shelf front collapses about 3 months later (<1 month before calving; Fig. 3e). The Wilkins RC experiences a weaker version of the sequence in the year before calving (starting <18 months before calving), which probably preconditioned extreme sea-ice losses in 2008, alongside supportive atmospheric conditions in winter 2007 to early 2008³⁹, which contrast with conditions that favoured sea-ice recovery in 2005⁴¹. The extreme sea-ice loss in 2008 includes the shortest perennial fast-ice lengths over the

record before calving, with $L_{per} < 1$ km on some days in April 2008, compared with (for example) $L_{per} > 5$ km in 2004 (Fig. 3g). There is also evidence of preconditioning in the year before calving for the Wilkins CL, starting (<18 months before the calving events) with the onset of a rapid decrease in pack-ice length from the end of December 2006 to mid-January 2007 and the subsequent removal of fast ice from March–June 2007 (Fig. 3h–i). Pack ice and annual fast ice return partially during winter 2007 (compared with previous years), such that the pack ice retreats early (starting December 2007, <6 months before the calving events) and rapidly, followed by fast-ice removal in January 2008, which does not recover until after the calving events.

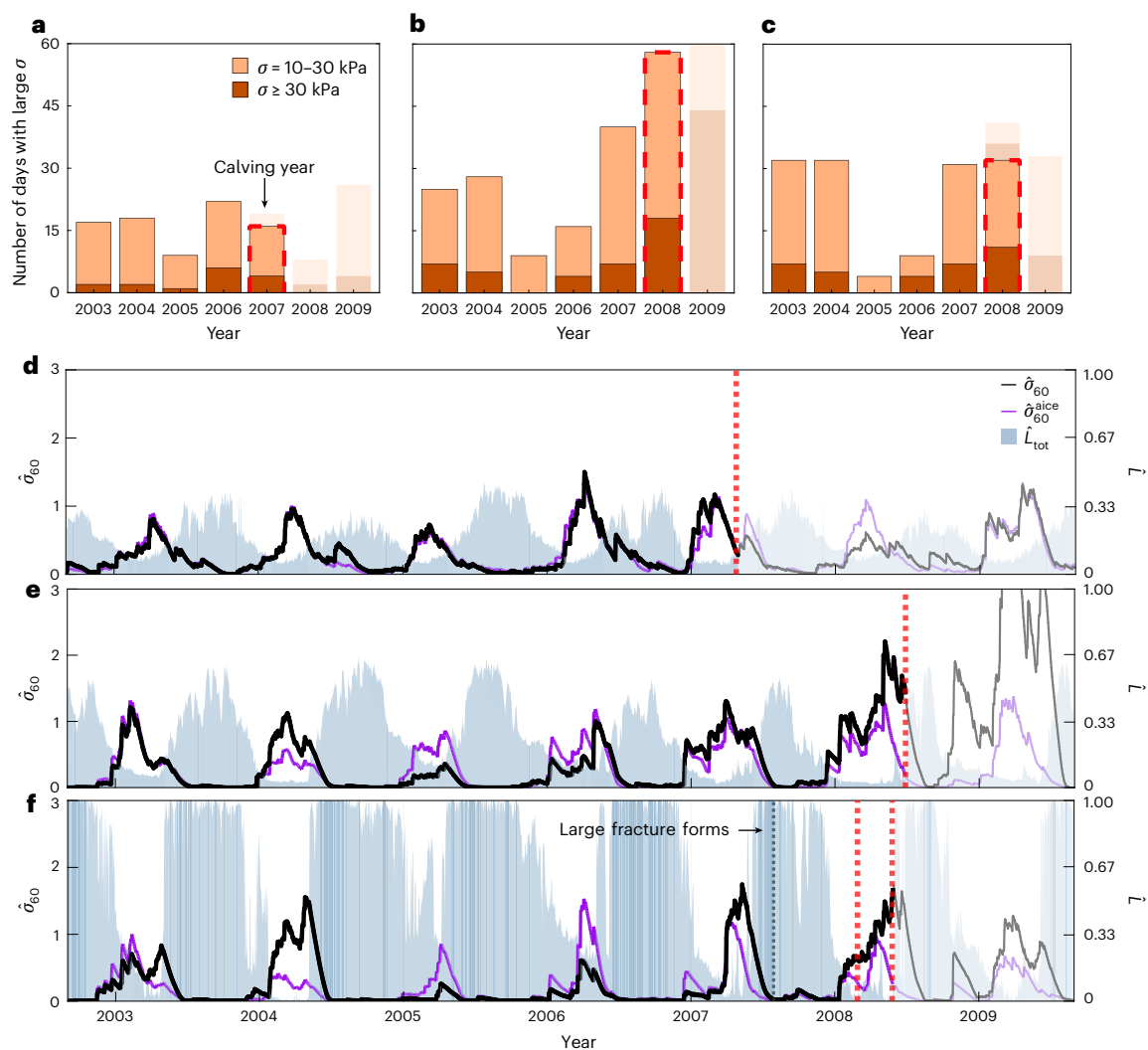


Fig. 4 | Flexural ice-shelf stress due to swell over 2003–2009. **a–c**, Number of days with $\sigma = 10\text{--}30$ kPa and $\sigma \geq 30$ kPa for the Voyeykov (**a**), Wilkins RC (**b**) and Wilkins CL (**c**). **d–f**, Daily time-series of 60-day accumulated stress values normalized by the average yearly maxima using daily sea-ice lengths (Fig. 3d–i) and daily median wave heights ($\hat{\sigma}_{60}$; black curves), for the Voyeykov (**d**), Wilkins RC (**e**) and Wilkins CL (**f**). Time-series using climatological sea-ice lengths (daily average over the 7-year record) and daily median wave heights ($\hat{\sigma}_{60}^{\text{aice}}$; purple

curves) are included to indicate where variations are driven by swell (black and purple curves are similar) or by sea-ice lengths (black and purple curves separate). Daily time-series of total sea-ice lengths normalized by the total transect length are shown in the background (L_{tot} ; shaded regions), where the transects extend to 10° N of the shelf fronts for Wilkins RC and Voyeykov, and 12° W for Wilkins CL (Methods). As in Fig. 3, the lighter shaded regions in **a–f** after the calving events.

Sustained durations of swell-induced flexure

The model predicts major increases in the number of days for which swell-induced flexural stress is estimated to exceed internal stress (≥ 30 kPa) and be comparable to it (10–30 kPa)³⁶ in the calving year and the year before (Fig. 4a–c), and noting that the model does not incorporate additional stress due to damage. The underlying daily time series is given for 60-day accumulated stress (Fig. 4d–f) to represent the importance of ice-shelf fatigue created by sustained swell impacts^{41,42–44}. For each shelf front, the yearly peaks (following summer and the sea-ice minima) are anomalously large and wide in both the year of the calving events and the year before. For the Voyeykov (Fig. 4d), the interannual variability from 2003–2006 is driven by incoming swell (black and purple curves are similar), including the largest overall peak in summer 2006 (<18 months before calving). In late 2006 (<6 months before calving), the 60-day accumulated stress normalized by the average yearly maximum ($\hat{\sigma}_{60}$) is >1 (that is, the accumulated stress is greater than its average yearly maximum) due to a rapid retreat of sea-ice length (black curve above purple), which lasts until mid-March 2007. In 2007, the Wilkins RC has $\hat{\sigma}_{60} > 1$ for approximately 2 weeks,

whereas Wilkins CL has $\hat{\sigma}_{60} > 1$ for ~2 months (both <18 months before calving; Fig. 4e,f). Following an early sea-ice retreat, Wilkins RC has $\hat{\sigma}_{60} > 1$ from January to mid-February 2008 (<6 months before calving), and then again from April until after the calving event, with a maximum of $\hat{\sigma}_{60} > 2$ in early May. The Wilkins CL has rapidly increasing accumulated stress at the beginning of 2008 (<6 months before the first calving), reaching $\hat{\sigma}_{60} \approx 0.7$ during February 2008 (<1 month before the first calving) and then increasing to $\hat{\sigma}_{60} \approx 1.7$ at the second calving event.

Conceptual model and implications

The findings are distilled into a conceptual model of the swell–sea-ice–shelf-front processes leading to the sustained flexure that we propose triggered the large-scale calving events (Fig. 5a). This model advances the conceptual model presented by Massom et al.¹¹ for the Larsen A, B and Wilkins disintegration events by emphasizing key timings, including fast ice, and separating the Wilkins RC and CL events. The processes are divided into preconditioning <18 months before calving, preconditioning <6 months before and triggering <1 month before.

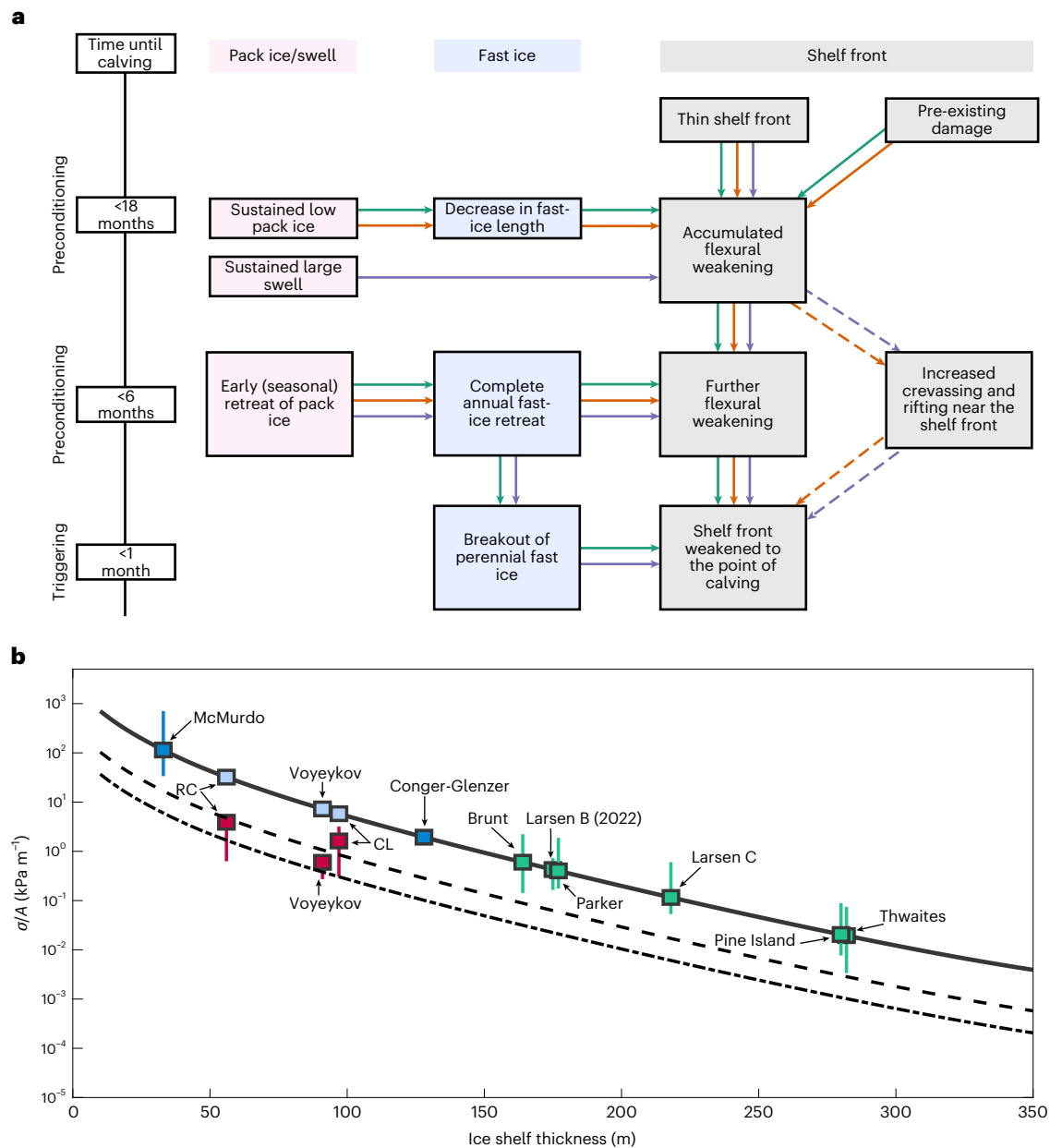


Fig. 5 | Conceptual model of swell–sea-ice–shelf front processes leading to large-scale calving events and instantaneous stress versus ice-shelf thickness. **a**, Processes are divided into preconditioning <18 months before calving, preconditioning <6 months before and triggering <1 month before, for pack ice and swell (pink boxes), fast ice (blue) and shelf fronts (grey). **b**, Flexural stress created by 12 s swell and normalized by the incident amplitude, A , versus ice-shelf thickness with no sea-ice barrier (solid black line), a 100-km pack-ice barrier (dashed) and a 100-km sea-ice barrier (60 km of pack ice, 20 km of perennial fast ice and 20 km of perennial fast ice; dash-dotted). The stress values for the ice shelves

highlighted in Fig. 1a are overlain (without sea-ice barriers; labelled data points), including the Wilkins and Voyeykov shelf fronts (light-blue squares) and results with median sea-ice barriers in the 60-day window before calving (red squares, with red lines denoting quartiles). Other ice shelves are included, with blue data points showing cases with reported thickness values (the square data points are the mean thickness and vertical lines are thickness ranges) and green data points showing thickness values calculated using CryoSat-2 data (the square data points represent the median thickness values and the lines are the quartiles).

The conceptual model encompasses the commonalities between the Wilkins RC, CL and Voyeykov, in terms of the reduced pack ice, the removal of fast ice and the shelf-front weakening. It also accounts for key differences, such as amplified flexure being driven by pack-ice loss for the Wilkins RC and CL versus large swell for the Voyeykov (Fig. 4d–f), and the absence of long-term perennial fast ice and the formation of a large fracture for the Wilkins CL (Figs. 2i and 3i).

Other large-scale calving events, such as McMurdo 2016 and Conger–Glenzer 2022, have been linked with sea-ice loss and swell-induced flexure^{19,45}. They seem to fit the conceptual model, as they

both involved thin ice shelves with fast ice attached to the shelf fronts, and they calved following prolonged reductions in their sea-ice barriers^{19,45}, although preconditioning in the year before calving is unknown. Without a sea-ice barrier, a large-amplitude 12 s swell could create flexural stress comparable to internal stress in the Conger–Glenzer ($\sigma/A \approx 2 \text{ kPa m}^{-1}$; Fig. 5b) and an amplitude of only 1 m would create flexural stress likely to exceed internal stress in the McMurdo ($\sigma/A > 30 \text{ kPa m}^{-1}$)^{35,36}. The McMurdo 2016 event is closest to the Wilkins RC/Voyeykov version of the model, as it calved over a heavily fractured area without a fast-ice barrier¹⁹, whereas the Conger–Glenzer

2022 event has aspects of both versions of the model, including amplification of a large fracture⁴⁵, as with the Wilkins CL. The Parker 2019 and Larsen B 2022 large-scale calving events have also been linked with sea-ice loss^{10,20}, and seem to be aligned with the conceptual model, despite being considerably thicker than the Wilkins and Voyeykov (such that $0.1 < \sigma/A < 1 \text{ kPa m}^{-1}$ without a sea-ice barrier; Fig. 5b). However, in general, the conceptual model does not apply to thicker ice shelves. For instance, there are no indications that the Larsen C 2017, Brunt 2023 or Brunt 2024 large-scale calving events are linked to sea-ice losses.

Our findings indicate that rapid and widespread Antarctic sea-ice loss will be an important factor in future large-scale calving events. Even a hypothesized extreme rate of thinning over the years studied for the Wilkins and Voyeykov has a far smaller impact on swell-induced flexure than the sea-ice losses they experienced (Extended Data Fig. 1). In terms of the instantaneous flexural stress in response to a 12 s swell, the median sea-ice barriers (2003–calving) for the Voyeykov and Wilkins RC approximately double their effective thickness (Fig. 5b). More generally, an effective sea-ice barrier ($L_{\text{tot}} = 100 \text{ km}$) is equivalent to an additional 50–100 m of ice-shelf thickness (for a 12 s swell; Fig. 5b). The context of each shelf front should also be considered—for instance, the thin McMurdo exists in a sheltered location that probably protects it from frequent large swell. Moreover, swell-induced stress will be amplified in fractures not captured in the model³⁰; note that glaciological stress was also amplified to ~200 kPa in fractures present on the Wilkins before calving³³, which is comparable to the largest of our predicted stress values (for median significant wave height values and without fractures). However, the rapidly thinning and weakening Pine Island and Thwaites^{46–48} still have a long way to go before swell-induced stress becomes a likely contributor to calving, even without sea-ice barriers (σ/A on the order of $10^{-2} \text{ kPa m}^{-1}$; Fig. 5b).

Online content

Any methods, additional references, Nature Portfolio reporting summaries, source data, extended data, supplementary information, acknowledgements, peer review information; details of author contributions and competing interests; and statements of data and code availability are available at <https://doi.org/10.1038/s41561-025-01713-4>.

References

- Qi, M. et al. A 15-year circum-Antarctic iceberg calving dataset derived from continuous satellite observations. *Earth Syst. Sci. Data* **13**, 4583–4601 (2021).
- Greene, C. A., Gardner, A. S., Schlegel, N. & Fraser, A. D. Antarctic calving loss rivals ice-shelf thinning. *Nature* **609**, 948–953 (2022).
- Davison, B. J. et al. Annual mass budget of Antarctic ice shelves from 1997 to 2021. *Sci. Adv.* **9**, eadi0186 (2023).
- Joughin, I., Shapero, D., Smith, B., Dutrioux, P. & Barham, M. Ice-shelf retreat drives recent Pine Island Glacier speedup. *Sci. Adv.* **7**, eabg3080 (2021).
- Marsh, O. J., Luckman, A. J. & Hodgson, D. A. Rapid acceleration of the Brunt Ice Shelf after calving of iceberg A-81. *Cryosphere* **18**, 705–710 (2024).
- Scambos, T., Hulbe, C. & Fahnestock, M. in *Antarctic Peninsula Climate Variability: Historical and Paleoenvironmental Perspectives* Antarctic Research Series Vol. 79 (eds Domack, E. et al) 79–92 (AGU, 2003).
- Braun, M. & Humbert, A. Recent retreat of Wilkins Ice Shelf reveals new insights in ice shelf breakup mechanisms. *IEEE Geosci. Remote Sens. Lett.* **6**, 263–267 (2009).
- Cook, A. J. & Vaughan, D. G. Overview of areal changes of the ice shelves on the Antarctic Peninsula over the past 50 years. *Cryosphere* **4**, 77–98 (2010).
- Arthur, F. R. et al. The triggers of the disaggregation of Voyeykov Ice Shelf (2007), Wilkes Land, East Antarctica, and its subsequent evolution. *J. Glaciol.* **67**, 933–951 (2021).
- Gomez-Fell, R., Wolfgang, R., Purdie, H. & Marsh, O. Parker Ice Tongue collapse, Antarctica, triggered by loss of stabilizing land-fast sea ice. *Geophys. Res. Lett.* **49**, e2021GL096156 (2022).
- Massom, R. A. et al. Antarctic ice shelf disintegration triggered by sea ice loss and ocean swell. *Nature* **558**, 383–389 (2018).
- Skvarca, P., Rack, W., Rott, H. & Donangelo, T. I. Evidence of recent climatic warming on the eastern Antarctic Peninsula. *Ann. Glaciol.* **27**, 628–632 (1998).
- Turner, J. T., Overland, J. E. & Walsh, J. E. An Arctic and Antarctic perspective on recent climate change. *Int. J. Climatol.* **27**, 277–293 (2007).
- Teder, N. J., Bennetts, L. G., Reid, P. A. & Massom, R. A. Sea ice-free corridors for large swell to reach Antarctic ice shelves. *Environ. Res. Lett.* **17**, 045026 (2022).
- Fox-Kemper, B. et al. in *Climate Change 2021: The Physical Science Basis* (eds Masson-Delmotte, V. et al.) 1211–1362 (IPCC, Cambridge Univ. Press, 2021).
- Squire, V. A. & Moore, S. C. Direct measurement of the attenuation of ocean waves by pack ice. *Nature* **283**, 365–368 (1980).
- Baker, M. G. et al. Seasonal and spatial variations in the ocean-coupled ambient wavefield of the Ross Ice Shelf. *J. Glaciol.* **65**, 912–925 (2019).
- Massom, R. A. et al. Examining the interaction between multi-year landfast sea ice and the Mertz Glacier Tongue, East Antarctica: another factor in ice sheet stability? *J. Geophys. Res. Oceans* **115**, 045026 (2010).
- Banwell, A. F. et al. Calving and rifting on the McMurdo Ice Shelf, Antarctica. *Ann. Glaciol.* **58**, 78–87 (2017).
- Ochwat, N. E. et al. Triggers of the 2022 Larsen B multi-year landfast sea ice breakout and initial glacier response. *Cryosphere* **18**, 1709–1731 (2024).
- Miles, B. W. J., Stokes, C. R. & Jamieson, S. S. R. Simultaneous disintegration of outlet glaciers in Porpoise Bay (Wilkes Land), East Antarctica, driven by sea ice break-up. *Cryosphere* **11**, 427–442 (2017).
- Cathles IV, L. M., Okal, E. A. & MacAyeal, D. R. Seismic observations of sea swell on the floating Ross Ice Shelf, Antarctica. *J. Geophys. Res. Earth Surf.* **114**, F02015 (2009).
- MacAyeal, D. R. et al. Transoceanic wave propagation links iceberg calving margins of Antarctica with storms in tropics and Northern Hemisphere. *Geophys. Res. Lett.* **33**, 2–5 (2006).
- Bromirski, P. D. et al. Ross Ice Shelf vibrations. *Geophys. Res. Lett.* **42**, 7589–7597 (2015).
- Fraser, A. D. et al. High-resolution mapping of circum-Antarctic landfast sea ice distribution, 2000–2018. *Earth Syst. Sci. Data* **12**, 2987–2999 (2020).
- Fraser, A. D. et al. Antarctic landfast sea ice: a review of its physics, biogeochemistry and ecology. *Rev. Geophys.* **61**, e2022RG000770 (2023).
- Meylan, M. H. et al. Dispersion relations, power laws, and energy loss for waves in the marginal ice zone. *J. Geophys. Res. Oceans* **123**, 3322–3335 (2018).
- Pitt, J. P. A. & Bennetts, L. G. On transitions in water wave propagation through consolidated to broken sea ice covers. *Proc. R. Soc. A* **480**, 20230862 (2024).
- Bennetts, L. G. & Meylan, M. H. Complex resonant ice shelf vibrations. *SIAM J. Appl. Math.* **81**, 1483–1502 (2021).
- Bennetts, L. G., Liang, J. & Pitt, J. P. A. Modeling ocean wave transfer to Ross Ice Shelf flexure. *Geophys. Res. Lett.* **49**, e2022GL100868 (2022).

31. Braun, M., Humbert, A. & Moll, A. Changes of Wilkins Ice Shelf over the past 15 years and inferences on its stability. *Cryosphere* **3**, 41–56 (2009).
 32. Scambos, T. et al. Ice shelf disintegration by plate bending and hydro-fracture: satellite observations and model results of the 2008 Wilkins Ice Shelf break-ups. *Earth Planet. Sci. Lett.* **280**, 51–60 (2009).
 33. Rankl, M., Fürst, J. J., Humbert, A. & Braun, M. H. Dynamic changes on the Wilkins Ice Shelf during the 2006–2009 retreat derived from satellite observations. *Cryosphere* **11**, 1199–1211 (2017).
 34. Fretwell, P. et al. Bedmap2: improved ice bed, surface and thickness datasets for Antarctica. *Cryosphere* **7**, 375–393 (2013).
 35. Bassis, J. N. & Walker, C. C. Upper and lower limits on the stability of calving glaciers from the yield strength envelope of ice. *Proc. R. Soc. A* **468**, 913–931 (2012).
 36. Bassis, J. N. et al. Stability of ice shelves and ice cliffs in a changing climate. *Annu. Rev. Earth Planet. Sci.* **52**, 221–247 (2024).
 37. Turner, J. et al. Antarctic sea ice increase consistent with intrinsic variability of the Amundsen sea low. *Clim. Dynam.* **46**, 2391–2402 (2016).
 38. Pope, J. O., Holland, P. R., Orr, A., Marshall, G. J. & Phillips, T. The impacts of El Niño on the observed sea ice budget of West Antarctica. *Geophys. Res. Lett.* **44**, 6200–6208 (2017).
 39. Massom, R. A., Reid, P. A., Stammerjohn, S. & Barreira, S. Sea-ice extent and concentration [in “State of the climate in 2008”]. *Bull. Am. Meteorol. Soc.* **90**, 113–121 (2008).
 40. Zhu, T. & Yu, J. Y. A shifting tripolar pattern of Antarctic sea ice concentration anomalies during multi-year La Niña events. *Geophys. Res. Lett.* **49**, e2022GL101217 (2022).
 41. Shein, K. A., Waple, A. M., Diamond, H. J. & Levy, J. M. State of the climate in 2005. *Bull. Am. Meteorol. Soc.* **86**, S92–S95 (2005).
 42. Vinogradov, O. G. & Holdsworth, G. Oscillation of a floating glacier tongue. *Cold Reg. Sci. Technol.* **10**, 263–271 (1985).
 43. Sergienko, O. V. Elastic response of floating glacier ice to impact of long-period ocean waves. *J. Geophys. Res. Earth Surf.* **115**, F04028 (2010).
 44. Ren, D. & Leslie, L. M. Effects of waves on tabular ice-shelf calving. *Earth Interact.* **18**, 1–28 (2014).
 45. Walker, C. C. et al. Multi-decadal collapse of East Antarctica’s Conger–Glenzer Ice Shelf. *Nat. Geosci.* **17**, 1240–1248 (2024).
 46. Bevan, S. L., Luckman, A. J., Benn, D. I., Adusumilli, S. & Crawford, A. Thwaites Glacier cavity evolution. *Cryosphere* **15**, 3317–3328 (2021).
 47. De Rydt, J., Reese, R., Paolo, F. S. & Gudmundsson, G. H. Drivers of Pine Island Glacier speed-up between 1996 and 2016. *Cryosphere* **15**, 113–132 (2021).
 48. Wild, C. T. et al. Rift propagation signals the last act of the Thwaites Eastern Ice Shelf despite low basal melt rates. *J. Glaciol.* **70**, e21 (2024).
- Publisher’s note** Springer Nature remains neutral with regard to jurisdictional claims in published maps and institutional affiliations.
- Open Access** This article is licensed under a Creative Commons Attribution-NonCommercial-NoDerivatives 4.0 International License, which permits any non-commercial use, sharing, distribution and reproduction in any medium or format, as long as you give appropriate credit to the original author(s) and the source, provide a link to the Creative Commons licence, and indicate if you modified the licensed material. You do not have permission under this licence to share adapted material derived from this article or parts of it. The images or other third party material in this article are included in the article’s Creative Commons licence, unless indicated otherwise in a credit line to the material. If material is not included in the article’s Creative Commons licence and your intended use is not permitted by statutory regulation or exceeds the permitted use, you will need to obtain permission directly from the copyright holder. To view a copy of this licence, visit <http://creativecommons.org/licenses/by-nc-nd/4.0/>.
- © The Author(s) 2025

Methods

Identification of ice-shelf damage

Satellite images (Figs. 1 and 2) are ASAR WSM imagery from ENVISAT, which operated from March 2002–April 2012. Owing to its all-weather, day–night imaging capability, ENVISAT ASAR WSM imagery is available in late autumn and winter, which covers the Wilkins and Voyeykov calving events. A basemap of Antarctica, its islands and the Voyeykov and Wilkins ice shelves was imported from the Making Earth System Data Records for Use in Research Environments (MEaSUREs) Antarctic Boundaries for International Polar Years 2007–2009 from Satellite Radar (Version 2)⁴⁹. We edited the Wilkins shelf fronts in the MEaSUREs Antarctic Boundaries dataset to match the ENVISAT ASAR WSM imagery. As the Voyeykov is unconfined and terminates into a widespread *mélange* layer, we edited its shelf-front locations in the MEaSUREs Antarctic Boundaries dataset to match those given by ref. 9. Fracture locations were identified using a method previously applied to the Voyeykov⁹ and the George VI⁵⁰. The method uses both ENVISAT ASAR WSM and Landsat-7 Enhanced Thematic Mapper Plus images, with fractures manually mapped in Quantum Geographic Information System (QGIS). For guidance, we used similar work undertaken to map fracture locations for the Wilkins from 1990–2008, using imagery from ENVISAT ASAR, the Advanced Land Orbit satellite and Terra Advanced Spaceborne Thermal Emission and Reflection Radiometer satellites^{7,31}.

The reported percentage changes in ice-shelf area due to calving were calculated by comparing the area of the ice shelf pre- and post-calving. This was achieved by comparing ice-shelf extents over different years using ENVISAT ASAR WSM imagery and manually drawing polygons in QGIS to represent the areas lost to calving. Extended Data Table 1 lists all ice-shelf images used in the study.

Sea-ice lengths

Reported sea-ice lengths (Fig. 3) were calculated from a combination of (1) sea-ice concentration data from the AMSR-E ASI sea-ice dataset⁵¹ and (2) fast-ice extent datasets from ref. 25. Sea-ice concentration data are given as a percentage of areal sea-ice cover per grid cell on the ocean surface at a spatial resolution of 3.125 km² and a daily frequency from June 2002–September 2011. The fast-ice dataset is a binary measure per grid cell at a spatial resolution of 1 km² and a 15-day frequency from March 2000–March 2018. The fast-ice dataset includes an Antarctic land mask, for which ice-shelf extents are updated every March²⁵. For consistency, we changed the Voyeykov shelf front in the fast-ice dataset to that given by ref. 9, and we updated the Wilkins land mask at each calving event in 2008. To pair the sea-ice and fast-ice datasets, we converted the fast-ice dataset to a 3.125 km² resolution (to match the AMSR-E grid). AMSR-E sea-ice outputs were imported into QGIS, which produced the sea-ice maps in Fig. 2, where the pack-ice boundaries are corrected for fast ice from the converted fast-ice dataset²⁵.

An algorithm to calculate the presence and age of fast ice and the location of the shelf fronts was applied to the sea-ice and fast-ice datasets on the 3.125 km² grid. For each shelf front:

- (i) On the first day of the fast-ice record (1 September 2000), a counter was initiated to track the number of continuous days fast ice is present in each grid cell.
- (ii) Starting from 1 September 2002, a daily output containing the coordinates of ocean, land (that is, islands and the ice sheet), ice shelf, shelf front, annual fast ice and perennial fast ice was generated. The ice-shelf edge coordinates were calculated by checking for ice-shelf cells adjacent to ocean or fast-ice cells.
- (iii) Repeat (ii) for each day until 31 August 2009.

The following algorithm was then applied to calculate the sea-ice lengths. For each shelf front and each day in the record:

- (a) Incorporate the coordinates generated by step (i) of the previous algorithm into the daily AMSR-E ASI sea-ice dataset. Define

pack ice as any cell with a sea-ice concentration of $\geq 15\%$. In case of a conflict in which two different types of ice or land are present in a cell, priority is given to land, followed by perennial fast ice, annual fast ice and then pack ice. All remaining unclassified cells are then classified as ocean.

- (b) A pair of cells is chosen, where one cell is along the shelf front and the other cell is 10° N of the mean shelf-front latitude and between 12° W and 5° E of the mean shelf-front longitude (Wilkins RC and Voyeykov) or 12° W of the mean shelf front longitude and between the coastline and 10° N of the mean shelf-front latitude (Wilkins CL) (the 10° N boundary was chosen to avoid sea ice that would contaminate the swell data). A straight line ‘transect’ was calculated between these two cells (white and orange lines in Extended Data Fig. 2a,c). This leads to a higher density of sea-ice transects towards the centre of the shelf fronts (Extended Data Fig. 2a,c).
- (c) Sea-ice data are extracted for each cell along the transect. If land is present, the transect is discarded.
- (d) The effective pack-ice, annual fast-ice and perennial fast-ice lengths along the transect, $L_{\text{pck}}^{(t)}$, $L_{\text{ann}}^{(t)}$ and $L_{\text{per}}^{(t)}$, respectively, are calculated. The effective pack-ice length is the sum of the cell lengths containing pack ice multiplied by the mean sea-ice concentration in those cells, whereas the effective fast-ice lengths are simply the sums of the cell lengths containing the relevant fast-ice type.
- (e) Repeat (b)–(d) for each possible pair of cells.

On a given day, the total effective sea-ice length for a particular transect is calculated as

$$L_{\text{tot}}^{(t)} \equiv L_{\text{pck}}^{(t)} + L_{\text{ann}}^{(t)} + L_{\text{per}}^{(t)} \quad (1)$$

For a chosen shelf front on a given day, the transects with the lowest third of $L_{\text{tot}}^{(t)}$ were considered as the weakest part of the sea-ice barrier. The daily values reported for L_{pck} , L_{ann} and L_{per} are the mean values corresponding to these transects (Fig. 3d–i). The daily L_{tot} was obtained from the sum of L_{pck} , L_{ann} and L_{per} . A total sea-ice length in which each of the transects used was first normalized by its total transect length was also used ($\bar{L}_{\text{tot}}^{(t)}$; Fig. 4d–f). The number of low sea-ice days in each year for which $L_{\text{tot}} < 100$ km, alongside days with $L_{\text{pck}} \leq 50$ km, are shown in Fig. 3a–c.

Incoming ocean swell

Peak periods (T_p) and significant wave heights (H_s) were extracted from the Collaboration for Australian Weather and Climate Research Wave (CAWCR) hindcast – aggregated collection⁵². The CAWCR hindcast was generated using the WaveWatch III v4.08 wave model, which is forced by hourly wind and uses daily sea-ice concentration data from the research data archive operated by the National Center for Atmospheric Research (NCAR) for pre-2011 data. The hindcast is from 1 January 1979 to the present, with hourly outputs on a 0.4° spatial grid of the ocean surface, which were converted to daily maximum values for H_s and T_p . The operational range extends to 78° S. We used swell data from the hindcast for sea-ice concentrations of $\leq 25\%$, as it is unaffected by the presence of sea-ice⁵³.

For each day over the 7-year record and each shelf front, incoming H_s and T_p were calculated from the hindcast as follows:

- (I) Obtain H_s and T_p for the hindcast cells contained within the bounds defined in (b) from the above algorithm (Extended Data Fig. 2a,c).
- (II) Retain the median H_s and T_p values.

This provided daily H_s and T_p time series for each shelf front (Extended Data Fig. 3).

Model of swell-induced shelf-front flexural stress

The model used to predict swell-induced flexural stress on the Wilkins and Voyeykov shelf fronts (Fig. 4) combines models of swell attenuation over distance due to sea-ice barriers (pack, annual fast and perennial fast)²⁸ with a model of ice-shelf flexure in response to incoming swell³⁰ (Extended Data Fig. 4). The models are two-dimensional (a horizontal ‘wave’ dimension and a depth dimension), time-harmonic and involve interactions between regular incident ocean waves of a prescribed amplitude (A_{inc}), wave period (T) and a sequence of the different ice covers. They are based on linear potential-flow theory for the water motions combined with thin-elastic-plate theory for the floating ice cover, where the Young’s modulus is set to be 6 GPa for the sea-ice barriers⁵⁴ and 8 GPa for the ice shelves⁵⁵.

A first model was used to predict the exponential attenuation over distance of the incident wave through the pack-ice region, such that the amplitude reduces to

$$A_{\text{pck}} \approx A_{\text{inc}} \exp(-\alpha_{\text{pck}} L_{\text{pck}} / C_{\text{pck}}), \quad (2)$$

where $\alpha_{\text{pck}}(T)$ is the attenuation coefficient. The ice cover was modelled as an array of floes with a thickness of 0.52 m and lengths randomized about a mean value of 500 m (ref. 56) and at an average concentration C_{pck} . Attenuation is produced by wave scattering at the floe edges and wave energy dissipation due to drag pressure⁵⁷, calculated using the Robinson–Palmer model, which gives a frequency dependence similar to observations²⁷ with a damping parameter of 13.5 Pa s m⁻¹ (refs. 11, 54, 58). The evolution of wave attenuation models, which started in the 1970s, is documented in multiple review articles (for example, refs. 59–61). Sensitivity studies have also been conducted, such as that in ref. 62. Three-dimensional versions of the model are available but at a far greater computational cost and without evidence of major differences in the predicted attenuation coefficients^{63,64}.

Annual and perennial fast-ice models were used to predict the reduction in the incident waves due to reflection at the fast-ice edges and the subsequent exponential attenuation of the waves over distance through the fast-ice regions⁶⁵, such that the wave amplitude reaching the shelf front is

$$A_{\text{per}} = a_{\text{per}} A_{\text{ann}} \exp(-\alpha_{\text{per}} L_{\text{per}}) \quad \text{where} \quad A_{\text{ann}} = a_{\text{ann}} A_{\text{pck}} \exp(-\alpha_{\text{ann}} L_{\text{ann}}), \quad (3)$$

a_{per} denotes the transmitted (non-reflected) components and α_{per} are the attenuation coefficients. The models are based on the one outlined in the seminal study by Fox and Squire⁶⁶, but include the Robinson–Palmer dissipation model for attenuation, as in ref. 67. The annual fast-ice thickness was set to 2 m (ref. 68) and the perennial fast-ice thickness was 11 m (refs. 18, 68).

An ice-shelf model was used to predict the vertical displacement of the ice shelf, $\eta(x)$, due to flexural-gravity waves, forced by the proportion of the incident wave that reaches the shelf front, such that

$$\eta(x) = A_{\text{per}} \hat{\eta}(x), \quad (4)$$

where $\hat{\eta}(x : T)$ denotes the displacement due to unit-amplitude forcing. The form of the model used was pioneered in refs. 42, 69, and has since been extended to include an Archimedean ice-shelf draught (90% of the ice thickness)⁷⁰ and varying spatial profiles of ice-shelf thickness and seabed bathymetry²⁹. The version of model used in this study has been validated in terms of the ratio of flexural-gravity-wave to incident-ocean-wave amplitudes observed on the Ross Ice Shelf³⁰. The model also predicts that swell is far more sensitive to changes in ice-shelf thickness than seabed variations³⁵.

The maximum flexural stress per wave period is calculated from the displacement, such that

$$\sigma = \left| \frac{EH}{2(1-\nu^2)} \eta'' \right|, \quad (5)$$

where E is Young’s modulus and $\nu = 0.3$ is Poisson’s ratio. Relative to the forcing amplitude, flexural stress tends to increase monotonically with wave period in the swell regime, and is negatively correlated with the shelf-front thickness⁵⁵. Owing to the underlying assumptions of plane stress and strain⁷¹, equation (5) is the only non-zero component of the stress tensor. Three-dimensional models that involve more non-zero components of the stress tensor are currently being developed^{72,73}. However, they require numerical solution methods, which would be prohibitively expensive for the present study, and it is not yet clear in which regimes 2D model predictions of stress require the additional spatial dimension.

For each shelf front and each day over the 7-year record, the model was applied to L_{pck} , C_{pck} , L_{ann} and L_{per} , which were derived as described above. The incident wave amplitude and period are set to be $A_{\text{inc}} = 0.5H_s$ and $T = T_p$ using the median significant wave height and peak period for the relevant shelf front and day, derived as described in the previous section.

Extended Data Fig. 2b,d shows model outputs corresponding to the highlighted Wilkins RC transects in Extended Data Fig. 2a,c. Exponential attenuation of swell through the sea-ice barriers is evident, along with amplitude drops at the fast-ice edges due to partial reflection of the incident waves²⁸. The attenuation rate per kilometre is greatest in the pack ice due to the broken nature of the ice cover, and the attenuation rate is greater in annual fast ice than perennial fast ice. In contrast, the thicker perennial fast ice creates a greater amplitude drop than the annual fast ice. Once the incident wave reaches the shelf front, it imparts flexural stress as it travels through the ice shelf. The stress is responsive to variations in ice-shelf thickness, with a thickness decrease causing a stress increase, although the peak stress is away from the shelf front where the stress values are sampled.

For each shelf front and each day, the flexural stress outputs were reduced to a single value, σ , by taking the mean over 1–2 km from the shelf front for each transect and taking the mean over the transects. The interval of stress locations was chosen to be close to the shelf front but far enough away to avoid the shelf front boundary layer caused by the free-edge conditions. The accumulated stress (Fig. 4) is the weighted sum

$$\sigma_N = \sum_{n=0}^{N-1} \frac{(N-n)[\sigma]_{\text{day}-n}}{N}, \quad (6)$$

that is, the stress summed over an N -day window, where the weight of the stress decreases linearly with age until it moves outside the window.

Results in Fig. 4d–f were obtained using 60-day windows, which balance the responsiveness of the accumulated stress to changes in daily stress and capture build-ups over time (Extended Data Fig. 5). The normalized daily accumulated stress ($\hat{\sigma}_{60}$; Fig. 4d–f) is the ratio of the accumulated stress to the mean yearly maximum stress over the 7-year record for the shelf front. Corresponding results for climatological sea-ice lengths are also given ($\hat{\sigma}_{60}^{\text{aice}}$), which were calculated using a daily climatological average of L_{pck} , L_{ann} and L_{per} and the same wave conditions as σ_{60} .

Topological altimetry

The CryoSat-2 Synthetic Aperture Radar Interferometry Level-2I processing baseline-E mode was used to obtain surface elevation data to calculate ice-shelf thicknesses. The CryoSat-2 satellite was launched on 8 April 2010, and provides coverage to 88° S on a 369-day repeat cycle. For each ice shelf, all available tracks were taken from 2014–2023 within

the ice-shelf boundaries from the MEaSURES Antarctic Boundaries for International Polar Years 2007–2009 from Satellite Radar, Version 2⁴⁹. To account for any ice-shelf growth, a 10 km buffer zone was allowed in front the shelf front. When processing, any elevation with an accompanying ≥ 30 dB of backscatter was removed, following ref. 74, before outlier elevations (e) were removed if they fell outside the range

$$e_{25} - 1.5 \times \text{IQR}, e_{75} + 1.5 \times \text{IQR}. \quad (7)$$

A tidal-height correction using the Circum-Antarctic Tidal Simulation⁷⁵, the ocean tide loading from the Finite Element Solutions 2004 tidal atlas⁷⁶ and geoid from Earth Gravitational Models 1996 were used to correct altimetry data for variations in freeboard elevation. Ice-shelf thicknesses were calculated following refs. 77,78, which used

$$h = \frac{(e - \delta)\rho_w}{\rho_w - \rho_i} + \delta, \quad (8)$$

where h is ice-shelf thickness, e as the freeboard elevation, δ is the firm air content⁷⁹, $\rho_w = 1,028 \text{ kg m}^{-3}$ is the water density and $\rho_i = 917 \text{ kg m}^{-3}$ is the ice density.

Individual grids were built for each ice shelf with a resolution of 3 km^2 at a yearly temporal resolution. This set-up was chosen to prevent erroneous readings due to nearby ice shelves from influencing the ice-shelf thickness output, and to reduce processing time and counteract a lower density of altimetry tracks near the edge of the ice shelf⁷⁷. The distance of each grid cell from the shelf front was calculated, with only grid cells within 20 km of the shelf front retained to represent the approximate area lost in each calving. Each grid cell from 2014–2023 was combined, using the IQR method to remove outliers, such as those that picked up the surrounding ice sheet or fast ice. Quartiles were calculated for each ice shelf analysed in Fig. 5b that did not have a defined pre-calving ice-shelf thickness.

Data availability

Data used to calculate sea-ice lengths, our combined sea-ice product and stress outputs are available from the Australian Antarctic Data Centre at <https://doi.org/10.26179/59ed-y877>. All external data used in this study are freely available. Daily AMSR2 ASI sea-ice concentration data for Antarctica are available from <https://data.seaice.uni-bremen.de/>. Fast-ice data²⁵ can be obtained from https://data.aad.gov.au/metadata/AAS_4116_Fraser_fastice_circumantarctic. ENVISAT ASAR WSM images are available from https://esar-ds.esa.int/socat/ASA_WSM_IP. Landsat-7 Enhanced Thematic Mapper Plus imagery is available from <https://earthexplorer.usgs.gov/>. The CryoSat-2 ice elevation dataset is available from <https://science-pds.cryosat.esa.int/>. CAWCR hindcast data are available from https://data-cbr.csiro.au/thredds/catalog/catch_all/CMAR_CAWCR-Wave_archive/CAWCR_Wave_Hindcast_aggregate/catalog.html.

Code availability

All codes for sea-ice lengths, the extraction of wave statistics and the ice-shelf stress model are available from the Australian Antarctic Data Centre at <https://doi.org/10.26179/59ed-y877>.

References

- Mouginot, J., Scheuchl, B. & Rignot, E. MEaSURES Antarctic Boundaries for IPY 2007–2009 from Satellite Radar, Version 2 (NSIDC, 2017); <https://doi.org/10.5067/AXE4121732AD>
- Holt, T. O., Glasser, N. F., Quincey, D. J. & Siegfried, M. R. Speedup and fracturing of George VI Ice Shelf, Antarctic Peninsula. *Cryosphere* **7**, 797–816 (2013).
- Melsheimer, C. & Spreen, G. AMSR-E ASI sea ice concentration data, Antarctic, version 5.4 (NetCDF). PANGAEA <https://doi.org/10.1594/PANGAEA.898400> (2020).
- Smith, G. A. et al. Global wave hindcast with Australian and Pacific Island focus: from past to present. *Geosci. Data J.* **8**, 34–33 (2020).
- Tolman, H. L. Treatment of unresolved islands and ice in wind wave models. *Ocean Model.* **5**, 219–231 (2003).
- Williams, T. D., Bennetts, L. G., Squire, V. A., Dumont, D. & Bertino, L. Wave-ice interactions in the marginal ice zone. Part 1: theoretical foundations. *Ocean Model.* **71**, 81–91 (2013).
- Liang, J., Pitt, J. P. A. & Bennetts, L. G. Pan-Antarctic assessment of ice shelf flexural responses to ocean waves. *J. Geophys. Res. Oceans* **129**, e2023JC020824 (2024).
- Kurtz, N. T. & Markus, T. Satellite observations of Antarctic sea ice thickness and volume. *J. Geophys. Res. Oceans* **117**, C08025 (2012).
- Bennetts, L. G. & Squire, V. A. On the calculation of an attenuation coefficient for transects of ice-covered ocean. *Proc. R. Soc. A* **468**, 136–162 (2012).
- Williams, T. D., Bennetts, L. G., Squire, V. A., Dumont, D. & Bertino, L. Wave-ice interactions in the marginal ice zone. Part 2: numerical implementation and sensitivity studies along 1D transects of the ocean surface. *Ocean Model.* **71**, 92–101 (2013).
- Squire, V. A. Ocean wave interactions with sea ice: a reappraisal. *Annu. Rev. Fluid Mech.* **52**, 37–60 (2020).
- Golden, K. M. et al. Modeling sea ice. *Not. Am. Math. Soc.* **67**, 1535–1555 (2020).
- Shen, H. H. Wave-in-ice: theoretical bases and field observations. *Phil. Trans. R. Soc. A* **380**, 20210254 (2022).
- Bennetts, L. G. & Squire, V. A. Model sensitivity analysis of scattering-induced attenuation of ice-coupled waves. *Ocean Model.* **45**, 1–13 (2012).
- Bennetts, L. G., Peter, M. A., Squire, V. A. & Meylan, M. H. A three-dimensional model of wave attenuation in the marginal ice zone. *J. Geophys. Res. Oceans* **115**, C12043 (2010).
- Montiel, F., Squire, V. A. & Bennetts, L. G. Attenuation and directional spreading of ocean wave spectra in the marginal ice zone. *J. Fluid Mech.* **790**, 492–522 (2016).
- Squire, V. A. A theoretical, laboratory, and field study of ice-coupled waves. *J. Geophys. Res. Oceans* **89**, 8069–8079 (1984).
- Fox, C. & Squire, V. A. Reflection and transmission characteristics at the edge of shore fast sea ice. *J. Geophys. Res. Oceans* **95**, 11629–11639 (1990).
- Squire, V. A. & Fox, C. On ice coupled waves: a comparison of data and theory. In *Proc. 3rd International Conference on Ice Technology* 269–280 (Computational Mechanics Publications, 1992).
- Langhorne, P. J. et al. Fast ice thickness distribution in the western Ross Sea in late spring. *J. Geophys. Res. Oceans* **128**, e2022JC019459 (2023).
- Fox, C. & Squire, V. A. Coupling between the ocean and an ice shelf. *Ann. Glaciol.* **15**, 101–108 (1991).
- Kalyanaraman, B., Bennetts, L. G., Lamichhane, B. & Meylan, M. H. On the shallow-water limit for modelling ocean-wave induced ice-shelf vibrations. *Wave Motion* **90**, 1–16 (2019).
- Bennetts, L. G., Williams, T. D. & Porter, R. A thin-plate approximation for ocean wave interactions with an ice shelf. *J. Fluid Mech.* **984**, A48 (2024).
- Papathanasiou, T. K. & Belibassakis, K. A. A nonconforming hydroelastic triangle for ice shelf modal analysis. *J. Fluid Mech.* **91**, 102741 (2019).
- Tazhimbetov, N., Almquist, M., Werpers, J. & Dunham, E. M. Simulation of flexural-gravity wave propagation for elastic plates in shallow water using an energy-stable finite difference method with weakly enforced boundary and interface conditions. *J. Comput. Phys.* **493**, 112470 (2023).

74. Siegfried, M. R., Fricker, H. A., Roberts, M., Scambos, T. A. & Tulaczyk, S. A decade of West Antarctic subglacial lake interactions from combined ICESat and CryoSat-2 altimetry. *Geophys. Res. Lett.* **41**, 891–898 (2014).
75. Padman, L., Fricker, H. A., Coleman, R., Howard, S. & Erofeeva, L. A new tide model for the Antarctic ice shelves and seas. *Ann. Glaciol.* **34**, 247–254 (2002).
76. Lyard, F., Lefevre, F., Letellier, T. & Francis, O. Modelling the global ocean tides: modern insights from FES2004. *Ocean Dynam.* **56**, 394–415 (2006).
77. Chuter, S. J. & Bamber, J. L. Antarctic ice shelf thickness from CryoSat-2 radar altimetry. *Geophys. Res. Lett.* **42**, 10721–10729 (2015).
78. Griggs, J. A. & Bamber, J. L. Antarctic ice-shelf thickness from satellite radar altimetry. *J. Glaciol.* **57**, 485–498 (2011).
79. Ligtenberg, S. R. M., Kuipers Munneke, P. & Van Den Broeke, M. R. Present and future variations in Antarctic firn air content. *Cryosphere* **8**, 1711–1723 (2014).

Acknowledgements

The work was supported by the Australian Antarctic Science Program (Project 4528). N.J.T. is funded by an Australian Government Research Training Program Scholarship administered by the University of Adelaide. L.B.G. and A.D.F. are supported by Australian Research Council (ARC) grant number DP240100325. L.G.B. is supported by ARC grant numbers FT190100404 and DP200102828. A.D.F. is supported by ARC grant numbers FT230100234, LP170101090 and LE220100103. P.A.R. was supported through the Australian Bureau of Meteorology and R.A.M. through the the Australian Antarctic Division. R.A.M. is supported by the ARC Special Research Initiative the Australian Centre for Excellence in Antarctic Science (grant number SR200100008). The work of P.A.R. and R.A.M. contributes to the Australian Government's Australian Antarctic Partnership Program. This project received grant funding from the Australian Government as part of the Antarctic Science Collaboration Initiative programme.

We acknowledge C. Melshiemer, G. Spreen, L. Padman, L. Carrère, F. Lyard, the European Space Agency, the USGS, CSIRO and BoM for making the AMSR-E ARTIST ASI sea-ice concentration data, the ENVISAT ASAR WSM imagery, Landsat-7 Enhanced Thematic Mapper Plus data, CAWCR ocean hindcast data, CryoSat-2 ice elevations and the corrections to elevation data freely available.

Author contributions

N.J.T. and L.G.B. conceptualized the study and wrote the original draft of the Article, including visualizations. N.J.T. was responsible for data curation, formal analysis, investigation, methodology and software. L.G.B., P.A.R. and R.A.M. supervised N.J.T. J.P.A.P. and L.G.B. contributed software to implement the mathematical models. A.D.F. contributed to the investigation of fast ice. T.A.S. contributed to the investigation of satellite images of ice shelves. L.G.B., R.A.M., P.A.R. and T.A.S. obtained funding for the project. All authors contributed to reviewing and editing the writing and approved the Article for submission.

Competing interests

The authors declare no competing interests.

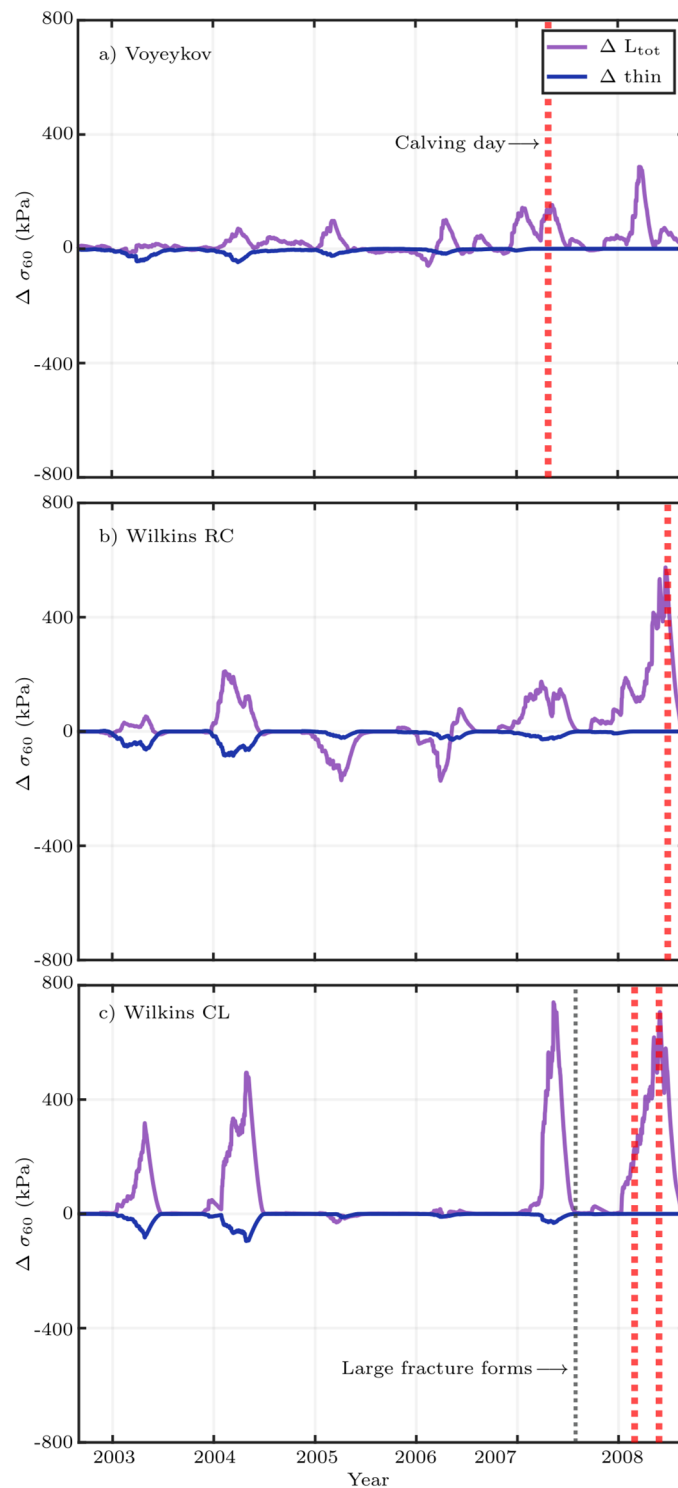
Additional information

Extended data is available for this paper at <https://doi.org/10.1038/s41561-025-01713-4>.

Correspondence and requests for materials should be addressed to Luke G. Bennetts.

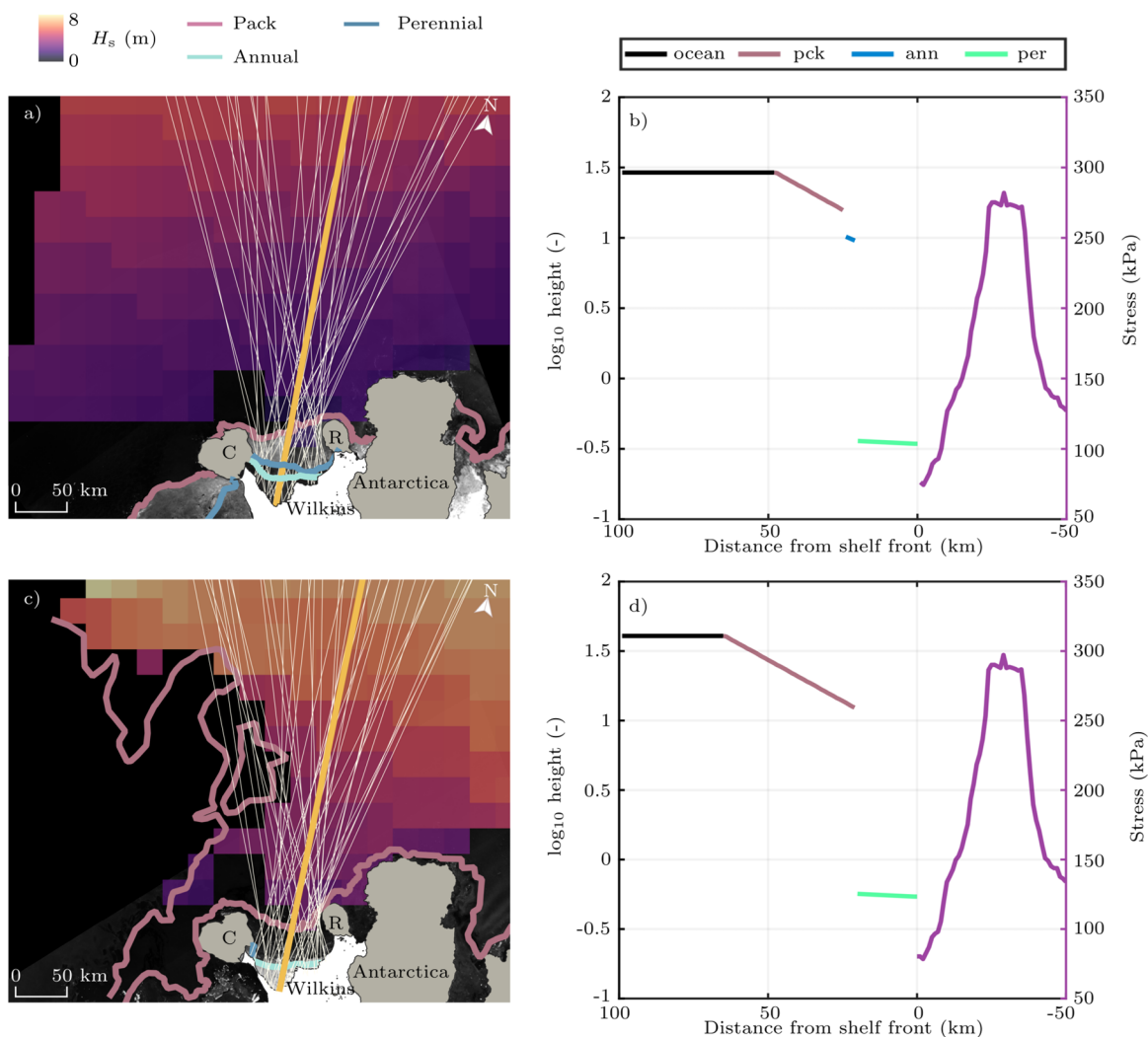
Peer review information *Nature Geoscience* thanks Rodrigo Felland the other, anonymous, reviewer(s) for their contribution to the peer review of this work. Primary Handling Editor: Thomas Richardson, in collaboration with the *Nature Geoscience* team.

Reprints and permissions information is available at www.nature.com/reprints.



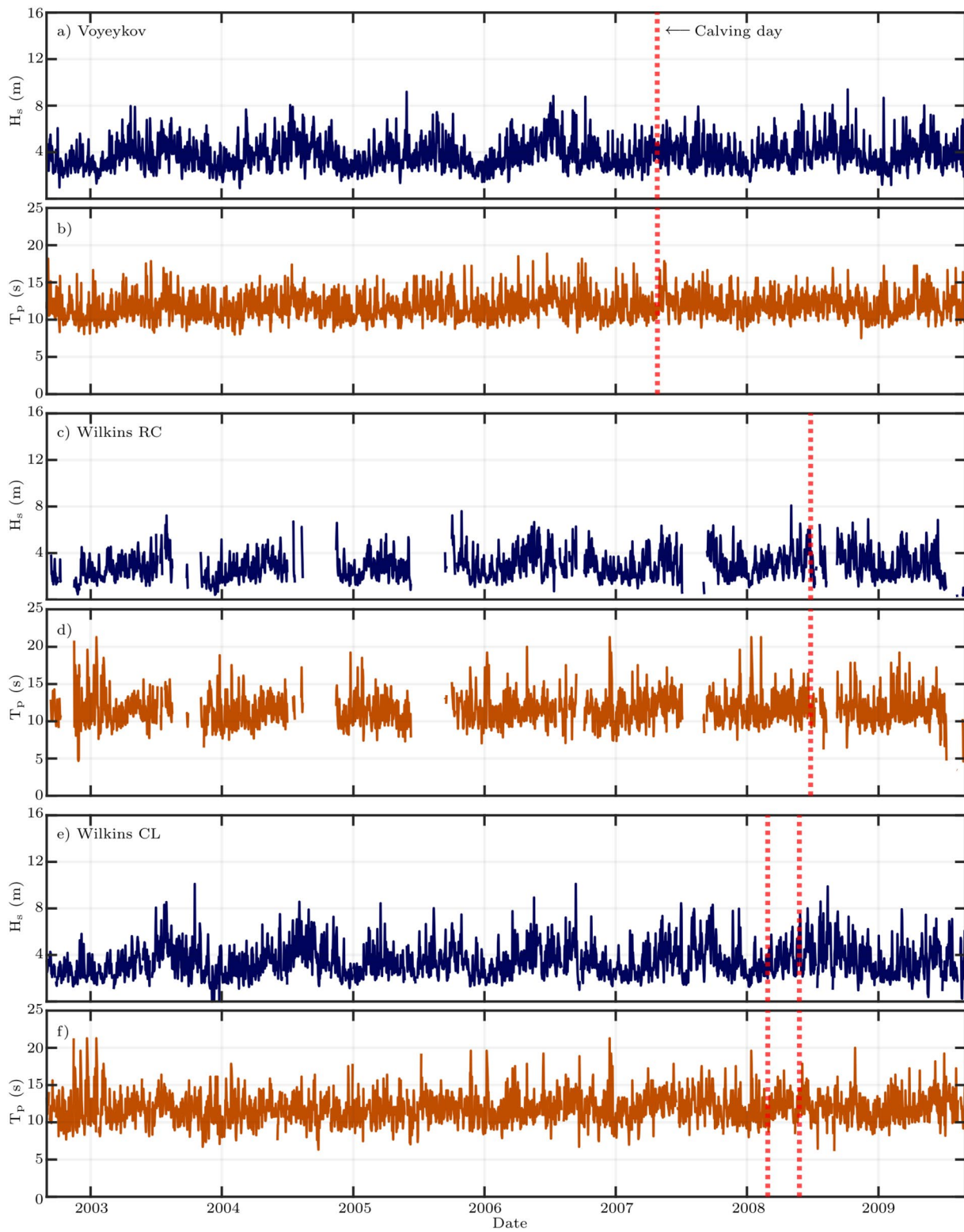
Extended Data Fig. 1 | Variations in accumulated stress due to hypothesised ice-shelf thinning, in addition to calculated sea-ice changes. (a–c) Daily time-series of $\Delta \sigma_{60} = \sigma_{60}^{ice} - \sigma_{60}$ over 2003–2008 for (a) Voyeykov, (b) Wilkins RC and (c) Wilkins CL. The reference accumulated stress (σ_{60}^{ice}) uses the mean daily sea-ice lengths and uniform-thickness ice shelves, where the thickness in the

calving year is consistent with the value at the location stress is sampled in the remainder of the study. The accumulated stress (σ_{60}) uses the calculated daily sea-ice lengths (purple curves) or ice-shelf thinning at a rate 1.5 m a^{-1} (blue), similar to the rapid thinning rate of the Thwaites Ice Shelf⁴⁶, and applied yearly (on 1 January).

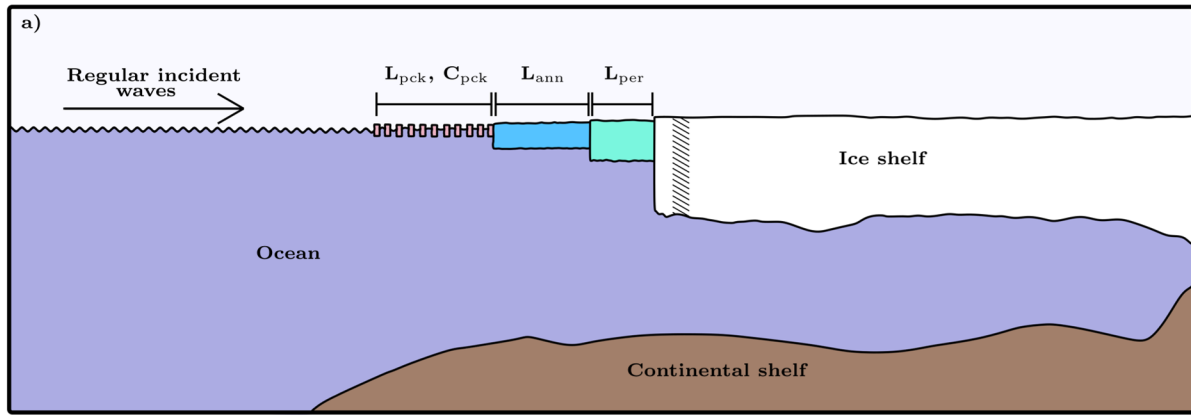


Extended Data Fig. 2 | Examples of transects used to calculate sea-ice lengths and model outputs. (a,c) Arbitrary selections of 40 transects (white lines; out of ≈ 9000) for the Wilkins RC on (a) 27 February 2007 and (c) 19 June 2008 (\approx one week before its large-scale calving event), with the underlying satellite image from ENVISAT ASAR WSM imagery, including lines for the outer boundaries of the pack-ice, annual fast-ice and perennial fast-ice barriers, and

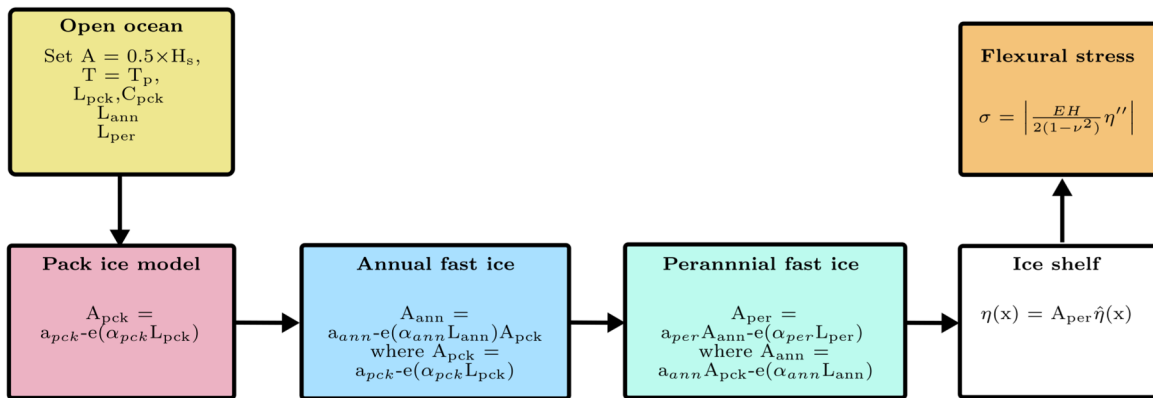
significant wave heights from the CAWCR hindcast⁵². (b,d) Model outputs for transects highlighted in the corresponding left-hand panels (thick orange lines), for the wave height in the sea-ice intervals showing attenuation over distance and drops at the fast-ice edges, and the resulting flexural stress on the Wilkins RC. The incoming swell have wave height and period (b) $H \approx 24 = 9.9$ m and $T = 14$ s, and (d) $H = 8.6$ m and $T = 11.6$ s, corresponding to the left-hand panels.



Extended Data Fig. 3 | Wave statistics for the Voyeykov, Wilkins RC and Wilkins CL. Daily time series for (a,c,e) significant wave height and (b,d,f) peak period for the (a,b) Voyeykov, (c,d) Wilkins RC and (e,f) Wilkins CL.

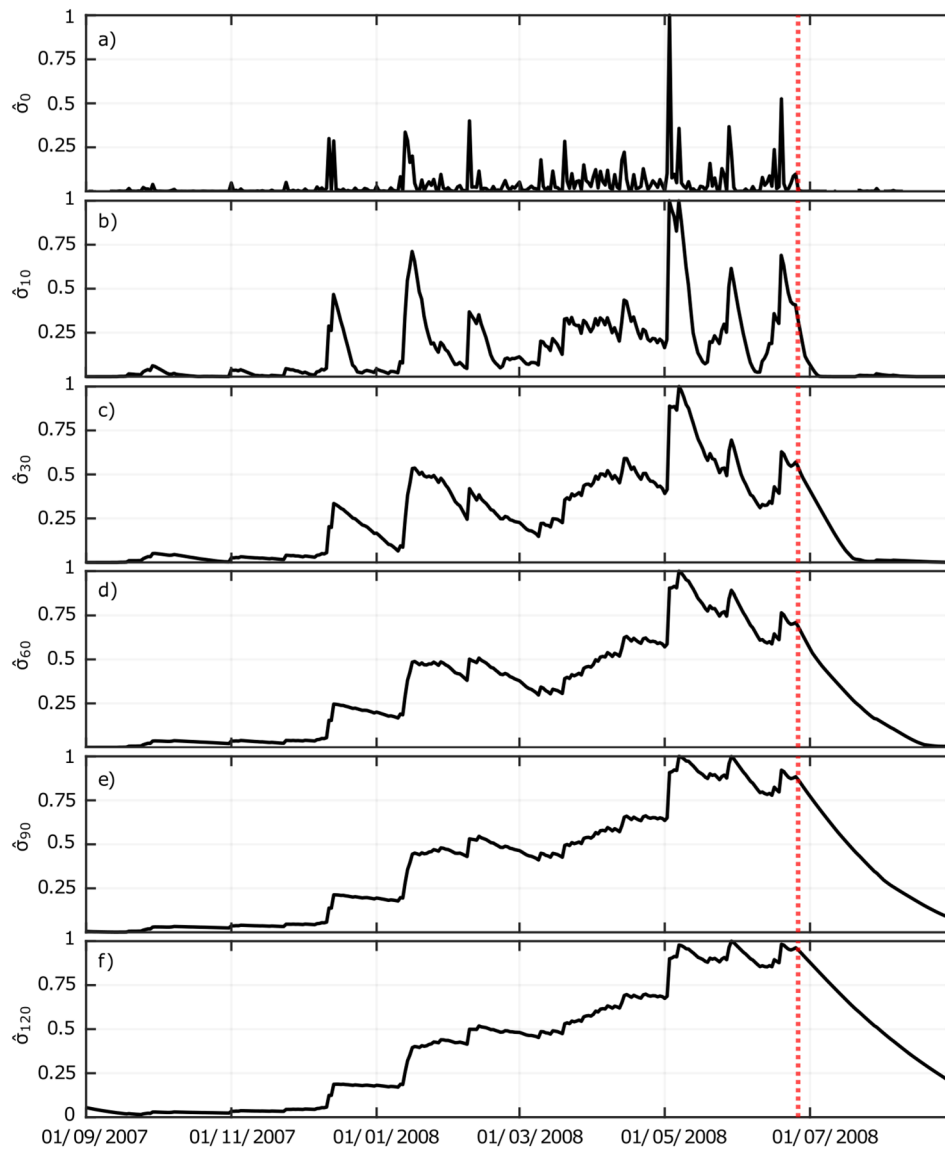


b)



Extended Data Fig. 4 | Model schematic and order of operations. (a) Regular incident waves interact with a sea-ice barrier, consisting of a pack-ice barrier with effective length L_{pck} , concentration C_{pck} and thickness 0.52 m, an annual fast-ice

barrier with length L_{ann} and thickness 2 m, and a perennial fast-ice barrier with length L_{per} and thickness 11 m, before interacting with the ice shelf. (b) Flow chart of the model with the order of operations.



Extended Data Fig. 5 | Sensitivity of normalised accumulated stress to window length. Example results for the Wilkins RC over 2007–2008 (around its calving event, indicated by the dotted red line), using six different choices of window length: (a) $N=0$, (b) 10 days, (c) 30 days, (d) 60 days, (e) 90 days and (f) 120 days.

Extended Data Table 1 | Envisat ASAR WSM and Landsat-8 images used in the study

Satellite	Date	Path	Row	Scene Identifier
Envisat ASAR	25/03/2004	-	-	ASA_WSM_1PNDSI20040325_123048_000001352025_00238_10813_0000
Envisat ASAR	29/03/2004	-	-	ASA_WSM_1PNDSI20040329_234824_000001592025_00302_10877_0000
Envisat ASAR	04/06/2004	-	-	ASA_WSM_1PNDSI20040604_052639_000000982027_00248_11825_0000
Envisat ASAR	18/03/2006	-	-	ASA_WSM_1PNDSI20060318_235141_000001352046_00073_21169_0000
Envisat ASAR	24/02/2007	-	-	ASA_WSM_1PNDSI20070224_122843_000000922055_00467_26072_0000
Envisat ASAR	14/04/2007	-	-	ASA_WSM_1PNDSI20070414_233113_000000922057_00173_26780_0000
Envisat ASAR	30/04/2007	-	-	ASA_WSM_1PNDSI20070430_232824_000000922057_00402_27009_0000
Envisat ASAR	28/06/2007	-	-	ASA_WSM_1PNDSI20070628_123114_000002692059_00238_27847_0000
Envisat ASAR	28/02/2008	-	-	ASA_WSM_1PNDSI20080228_123200_000003612066_00238_31354_0000
Envisat ASAR	28/02/2008	-	-	ASA_WSM_1PNDSI20080228_123200_000003612066_00238_31354_0000
Envisat ASAR	19/06/2008	-	-	ASA_WSM_1PNDSI20080619_120700_000003922069_00338_32957_00000
Envisat ASAR	03/08/2008	-	-	ASA_WSM_1PNDSI20080803_052313_000001102070_00477_33597_00000
Landsat-7	29/02/2000	95	107	LE07.L2SR_096107_20000229_20200918_02.T2_SR
Landsat-7	09/11/2001	95	106	LE07.L2SR_095106_20011209_20200917_02.T2_SR
Landsat-7	09/11/2001	95	107	LE07.L2SR_095107_20011209_20200917_02.T2_SR
Landsat-7	05/12/2002	222	109	LE07.L2SR_222109_20021205_20200916_02.T2_SR
Landsat-7	05/12/2002	222	110	LE07.L2SR_222110_20021205_20200916_02.T2_SR
Landsat-7	05/12/2002	222	109	LE07.L2SR_222109_20060130_20200914_02.T2_SR
Landsat-7	30/01/2006	222	109	LE07.L2SR_222109_20060130_20200914_02.T2_SR
Landsat-7	15/01/2007	96	107	LE07.L2SR_096107_20070115_20200913_02.T2_SR
Landsat-7	26/01/2007	221	109	LE07.L2SR_221109_20070126_20200913_02.T2_SR
Landsat-7	16/02/2007	96	107	LE07.L2SR_096107_20070216_20200913_02.T2_SR
Landsat-7	28/02/2008	223	109	LE07.L2SR_223109_20080228_20200912_02.T2_SR
Landsat-7	28/02/2008	223	110	LE07.L2SR_223110_20080228_20200912_02.T2_SR